Itinerant ferromagnetism mediated by giant spin polarization of the metallic ligand band in the van der Waals magnet Fe5 Ge Te2

Letter

Itinerant ferromagnetism mediated by giant spin polarization of the metallic ligand band in the van der Waals magnet Fe_5GeTe_2

K. Yamagami,[1,2] Y. Fujisawa,[1] B. Driesen,[1] C. H. Hsu,[1,3] K. Kawaguchi,[2] H. Tanaka,[2] T. Kondo,[2] Y. Zhang,[4] H. Wadati,[5,6] K. Araki,[7] T. Takeda,[7] Y. Takeda,[8] T. Muro,[9] F. C. Chuang,[3,10,11] Y. Niimi,[12,13] K. Kuroda,[2] M. Kobayashi,[6,14] and Y. Okada[1]

[1]*Okinawa Institute of Science and Technology Graduate University, Onna-son, Kunigami-gun, Okinawa 904-0495, Japan*
[2]*Institute for Solid State Physics, The University of Tokyo, Kashiwa, Chiba 277–8581, Japan*
[3]*Department of Physics, National Sun Yat-sen University, Kaohsiung 80424, Taiwan*
[4]*Institute of High Energy Physics, Chinese Academy of Sciences, Shijingshan District, Beijing 100049, China*
[5]*Graduate School of Material Science, University of Hyogo, Ako, Hyogo 678–1297, Japan*
[6]*Institute of Laser Engineering, Osaka University, Suita, Osaka 565–0871, Japan*
[7]*Department of Electrical Engineering and Information Systems, Graduate School of Engineering, The University of Tokyo, Bunkyo-ku, Tokyo 113–8656, Japan*
[8]*Materials Sciences Research Center, Japan Atomic Energy Agency, Sayo-cho, Sayo-gun, Hyogo 679–5148, Japan*
[9]*Japan Synchrotron Radiation Research Institute (JASRI), Sayo-cho, Sayo-gun, Hyogo 679–5198, Japan*
[10]*Department of Physics, National Tsing Hua University, Hsinchu 30013, Taiwan*
[11]*Physics Division, National Center for Theoretical Sciences, Hsinchu 30013, Taiwan*
[12]*Department of Physics, Graduate School of Science, Osaka University, Toyonaka 560–0043, Japan*
[13]*Center for Spintronics Research Network, Osaka University, Toyonaka 560–8531, Japan*
[14]*Center for Spintronics Research Network, The University of Tokyo, Bunkyo-ku, Tokyo 113–8656, Japan*

(Received 24 July 2020; revised 23 October 2020; accepted 7 January 2021; published 12 February 2021)

We investigate near-Fermi-energy (E_F) element-specific electronic and spin states of ferromagnetic van der Waals (vdW) metal Fe_5GeTe_2. The soft x-ray angle-resolved photoemission spectroscopy (SX-ARPES) measurement provides spectroscopic evidence of localized Fe 3*d* band. We also find prominent hybridization between the localized Fe 3*d* band and the delocalized Ge/Te *p* bands. This picture is strongly supported from direct observation of the remarkable spin polarization of the ligand *p* bands near E_F, using x-ray magnetic circular dichroism (XMCD) measurements. The strength of XMCD signal from ligand element Te shows the highest value, as far as we recognize, among literature reporting finite XMCD signal for nonmagnetic element in any systems. Combining SX-ARPES and elemental selective XMCD measurements, we collectively point to an important role of giant spin polarization of the delocalized ligand Te states for realizing itinerant long-range ferromagnetism in Fe_5GeTe_2. Our finding provides a fundamental elemental selective viewpoint for understanding mechanism of itinerant ferromagnetism in low-dimensional compounds, which also leads to insight for designing exotic magnetic states by interfacial band engineering in heterostructures.

DOI: 10.1103/PhysRevB.103.L060403

Understanding the mechanism of ferromagnetism in metals has been a longstanding nontrivial issue in a wide variety of condensed-matter systems. Based on the conventional itinerant picture, the so-called Stoner model explains the mechanism of itinerant ferromagnetism [1]. For example, in the transition metal Ni, a spin-polarized band with exchange band splitting emerges below the Currie temperature (T_C) [2,3]. This picture supports ferromagnetism arisen from the simple itinerant Ni 3*d* state. On the other hand, Fe shows persistent exchange band splitting above T_C [4]. This picture supports the localized nature of Fe 3*d* states rather than the simple itinerant picture. In complexed ferromagnetic metal compounds, the situation becomes richer [5,6]. For example, MnP shows band deformation across T_C, in line with the Stoner picture, with nontrivial pseudogap formation near Fermi energy (E_F) at low temperature [5]. In $SrRuO_3$, a violation of the Stoner picture is reported, with band renormalization with strong coupling to bosonic mode near E_F [6]. Regardless of material-dependent complications and richness, the most essential question for understanding ferromagnetism in metals has been clarifying whether an orbital with magnetic moment should be viewed as a localized or itinerant picture in many cases.

Owing to rapidly increasing interest in searching for novel magnetism in van der Waals (vdW) compounds, one particularly important challenge is understanding mechanism of itinerant ferromagnetism with reduced dimension [7–12]. Recent studies in vdW ferromagnetic metal Fe_3GeTe_2 ($T_C \sim 220$ K) supports localized nature of Fe 3*d* states [13]. However, this picture is not easily understood based on the so-called Mermin-Wagner theorem since this theorem does not allow long-range ferromagnetism starting from localized isotropic Heisenberg spins in two dimensions [14]. To reconcile, investigation on vdW ferromagnetic insulators $Cr_2Ge_2Te_6$ [15–19] and CrI_3 [20–22] provides useful insight. In these systems, the ligand states significantly

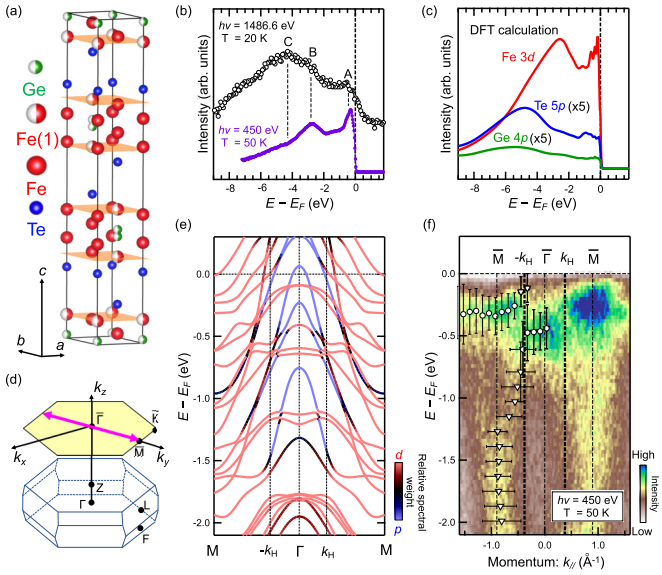

FIG. 1. (a) Crystal structure of Fe_5GeTe_2 depicted by VESTA [28]. 50% occupation for Fe(1) and Ge sites is known [27]. (b) The valence-band PES spectra at the incident photon energy ($h\nu$) of 1486.6 and 450 eV. See main body for details of the spectral features indicated by A–C. (c) The DFT-calculated partial density of states, multiplied by Fermi Dirac function. (d) The bulk and projected Brillouin zones of Fe_5GeTe_2. (e) The DFT calculation for relative spectral weight between d and p orbitals. (f) Photoemission intensity plot along $\bar{\Gamma}$-$\bar{\mathrm{M}}$ at 50 K and $h\nu = 450$ eV.

contribute to the ferromagnetism through hybridization with the orbital having magnetic moment [18,19,21,22]. Thus, this information provides a motivation of clarifying metallic vdW ferromagnet with an elemental selective point of view, particularly focusing on a role of ligand state. However, lacking direct investigation of elemental specific electronic and spin states hinders understanding of the mechanisms of emergent ferromagnetism in metallic vdW ferromagnets so far.

Here, we investigate the elemental selective valence-band electronic and spin states of Fe_5GeTe_2, using soft x-ray angle-resolved photoemission spectroscopy (SX-ARPES) [23] and soft x-ray magnetic circular dichroism (XMCD) in x-ray absorption spectroscopy (XAS) [24]. Fe_5GeTe_2, on which we focus, is an especially important itinerant ferromagnetic vdW compound due to its highest $T_C \sim 310$ K within existing metallic vdW ferromagnet [25–28]. The crystal structure of Fe_5GeTe_2 [as in Fig. 1(a)] is a hexagonal lattice with three Fe_5GeTe_2 layers in the unit cell. This paper provides clarification of elemental specific near E_F electronic and spin states in Fe_5GeTe_2. Our findings coherently point out that the remarkably large spin-polarized metallic ligand Ge/Te states play a major role for mediating itinerant long-range ferromagnetism in this vdW compound, providing a fundamental viewpoint for understanding of the emergence of itinerant ferromagnetism in low-dimensional systems.

A quenched single-crystal Fe_5GeTe_2 was synthesized in an evacuated quartz tube with an I_2 transport agent, as described in literature [26]. The temperature-dependent magnetic susceptibility measurement gives $T_C \approx 310$ K for our sample. The SX-ARPES measurements were performed at BL25SU of SPring-8 [29], and the incident photon energy ($h\nu$) was set to 450 eV with energy resolution of ~50 meV. Thanks to the smaller beam spot size, the observed band dispersion in SX-ARPES is slightly sharper than vacuum ultraviolet (VUV)-ARPES by He discharge lamp, related to the $\sqrt{3} \times \sqrt{3}$ domain structure [26], even if the energy resolution is much better for the latter case (see Fig. S1 in the Supplemental Material [30]). The XAS and XMCD measurements were performed at BL23SU of SPring-8 [31]. The details of experimental conditions for SX-ARPES, XAS, and XMCD are described in the Supplemental Material [26,27,29–31].

We first present capability of orbital selective photoemission spectroscopies (PES), based on $h\nu$ dependence of the photoionization cross section (σ_{nl}) and density-functional theory (DFT)-based partial density of states (PDOS) calculations. Figure 1(b) shows PES spectrum with both $h\nu = 1486.6$ eV (black line with empty symbol) and $h\nu = 450$ eV (purple line filled symbol). For both spectra, we observe three characteristic peak features labeled as A ($E - E_F \approx -0.5$ eV), B ($E - E_F \approx -2.8$ eV), and C ($E - E_F \approx -4.3$ eV). However, relative peak intensity largely depends on $h\nu$. In PES with $h\nu = 1486.6$ eV, peak feature C dominates rather than A and B, and overall spectral shape is similar to calculated PDOS for Ge $4p$ and/or Te $5p$ [see blue and green curves in Fig. 1(c)]. On the other hand, the spectrum with $h\nu = 450$ eV shows predominant peaks A and B, and overall spectral shape matches very well with calculated PDOS for Fe $3d$ [see the red curve in Fig. 1(c)]. These orbital selective PES spectra can be consistently understood based on $h\nu$ dependence of σ_{nl}. At $h\nu = 1486.6$ eV, σ_{nl} for the Fe $3d$, Te $5p$, and Ge $4p$ are $\sigma_{\mathrm{Fe}3d}/\sigma_{\mathrm{Te}5p} \simeq 0.55$ and $\sigma_{\mathrm{Fe}3d}/\sigma_{\mathrm{Ge}4p} \simeq 0.97$, while at $h\nu = 450$ eV, their relation represents $\sigma_{\mathrm{Fe}3d}/\sigma_{\mathrm{Te}5p} \simeq 4.7$ and $\sigma_{\mathrm{Fe}3d}/\sigma_{\mathrm{Ge}4p} \simeq 10$ [32]. Therefore, the Ge/Te-derived signal reasonably becomes more prominent using $h\nu = 1486.6$ eV whereas Fe $3d$-derived signature becomes more prominent with $h\nu = 450$ eV.

The experimental SX-ARPES ($h\nu = 450$ eV) at 50 K simply captures the most essential electronic feature seen in DFT calculation. Figure 1(e) shows calculated relative spectral weight contribution between d and p states on high-symmetry line along the $\bar{\Gamma}$-$\bar{\mathrm{M}}$ direction [the pink arrow in Fig. 1(d)]. Here, as in Fig. 1(c), d and p contributions mainly originate from Fe $3d$- and Te $5p$-derived states, respectively. The photoemission intensity image along the $\bar{\Gamma}$-$\bar{\mathrm{M}}$ direction is shown in Fig. 1(f). Less dispersive spectral weight distribution is seen (plotted with circle) around $\bar{\Gamma}$ and $\bar{\mathrm{M}}$ points, with disconnected spectral weight distribution around characteristic momentum $|k_{\mathrm{H}}| = 0.38$ Å^{-1}. On the other hand, a metallic holelike band is also observed around the $\bar{\Gamma}$ point (plotted with triangle). Combining SX-ARPES and DFT calculation, experimental flat distribution of spectral weight can be assigned as convolution of *multiple* Fe $3d$ bands. Also, the hole band around the $\bar{\Gamma}$ point is assigned as Ge/Te p band. More pronounced intensity for Fe $3d$ bands than delocalized Ge/Te p hole bands is consistently understood due to cross section σ_{nl} at $h\nu = 450$ eV. Furthermore, as shown by vertical broken lines in Fig. 1(e), experimental observation of disrupted spectral weight distribution across $\pm k_{\mathrm{H}}$ is qualitatively consistent with prominent hybridization around this momentum [33].

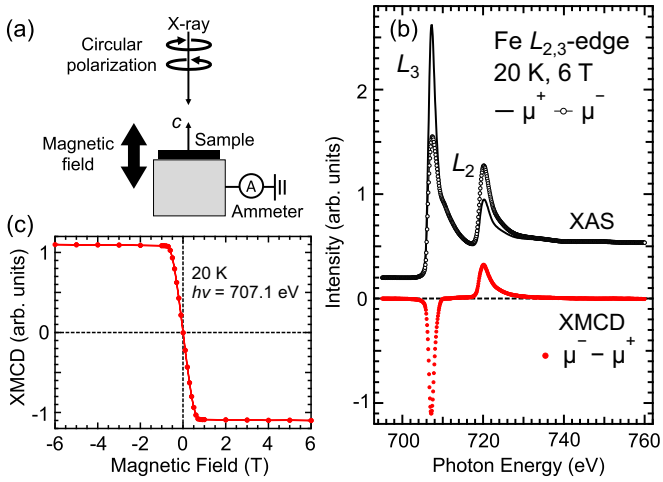

FIG. 2. (a) The experimental geometry of XAS/XMCD measurements in total electron yield (TEY) mode. See method part for details. (b) The Fe $L_{2,3}$-edge XAS and XMCD spectra at 20 K under 6 T. The $\mu^+(\mu^-)$ denotes the XAS absorption intensity for parallel (antiparallel) alignment of the photon helicity and the sample magnetization direction. (c) The magnetic field dependence of the XMCD intensity of Fe L_3 (707.1 eV) at the photon energy of the XMCD peak.

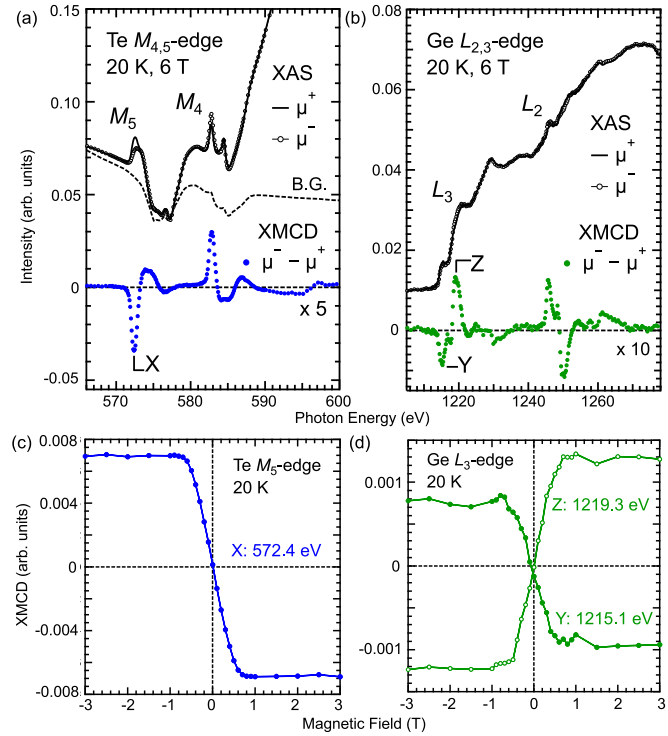

FIG. 3. (a), (b) The Te $M_{4,5}$-edge and Ge $L_{2,3}$-edge XAS and XMCD spectra of Fe_5GeTe_2 at 20 K under 6 T. In Te $M_{4,5}$ edge, the background spectrum including in the Cr $L_{2,3}$ edge ($\approx$ 576 and 585 eV) absorption from the focusing mirrors are shown as the black solid line. (c), (d) The element-specific magnetization curves of Te and Ge with the photon energy set at the XMCD peaks; X (572.4 eV), Y (1215.1 eV), and Z (1219.3 eV).

The elemental selective XMCD measurement is particularly powerful for magnetic systems with complicated band structure, such as in Fe_5GeTe_2. The XMCD signal is proportional to moment M for magnetic element. For nonemagnetic element, XMCD signal is proportional to the number of electrons with opposite spins $N(\uparrow_{\text{major}}) - N(\downarrow_{\text{minor}})$ from spin-polarized Ge/Te-derived bands. If the Ge/Te p band magnetically couples with the flat Fe $3d$ band through the hybridization, the itinerant Ge/Te p-derived orbitals near E_F are expected to provide finite XMCD signals.

Based on selection rule and orbital nature, the Fe $L_{2,3}$ edge corresponds to a $2p \rightarrow 3d$ excitation process. Then, the magnetic signal from Fe $3d$-derived states is first presented from Fe $L_{2,3}$-edge XAS and XMCD spectra, whose experimental geometry are shown in Fig. 2(a). Figure 2(b) shows the Fe $L_{2,3}$-edge XAS (μ^+ and μ^-) and XMCD (μ^-–μ^+) spectra at 20 K under a magnetic field of 6 T. The $\mu^+(\mu^-)$ denotes the XAS absorption intensity for parallel (antiparallel) alignment of the photon helicity and the sample magnetization direction. The metallic XAS spectral shape is consistent with hybridization-driven finite Fe $3d$-derived states at E_F [31,34], which is further supported by core-level PES spectra (see Fig. S2 in the Supplemental Material [30,35–43]). Figure 2(c) shows the magnetic field dependence of the XMCD intensity at the photon energy of 707.1 eV. Note here that three different Fe sites exist in Fe_5GeTe_2, as shown in Fig. 1(a). We find that the XMCD signal was overlapped from all three Fe sites in energy, and the signal is expected to be integral from three Fe sites. Indeed, the elemental-specific magnetization curve shape shown in Fig. 2(c) represents a small coercive field with saturation field 0.6 T, which is similar to magnetic curve seen in bulk measurement [26,27]. In addition to the calculated orbital and spin moment of $m_{\text{orb}} = 0.1\,\mu_B$/Fe and $m_{\text{spin}} = 1.8\,\mu_B$/Fe, the estimated total moment of $m_{\text{total}} = m_{\text{orb}} + m_{\text{spin}} = 1.9\,\mu_B$/Fe for 6 T, using the XMCD sum rules (see Fig. S3 in Supplemental Material [30,34,44,45]), is nearly identical to that from macroscopic magnetometry [27].

Spin-polarized signal from Te/Ge-derived orbitals have also been observed by XMCD. Figures 3(a) and 3(b) represent the Te $M_{4,5}$-edge Ge $L_{2,3}$-edge XAS and XMCD spectra taken at 20 K under a magnetic field of 6 T. Based on selection rule and orbital natures, the Te $M_{4,5}$ edge and Ge $L_{2,3}$ edge can be regarded as excitations of $3d \rightarrow 5p$ and $2p \rightarrow 4s/4d$, respectively. The magnetic field dependence of the XMCD signal for Te (at 572.4 eV labeled as X) and Ge (at 1215.1 and 1219.3 eV, labeled as Y and Z) are shown in Figs. 3(c) and 3(d), respectively. This is an observation of spin-polarized ligand Ge/Te states in Fe-Ge-Te vdW ferromagnets. Importantly, one can further see the sign change of the XMCD signal depending on elements and their excitation process.

To confirm the hybridization picture, we plot the magnetic field dependence of XMCD signals normalized at the saturated value of each absorption edges in Fig. 4(a). Note that the magnetic behavior of Ge/Te states is qualitatively identical to that of the Fe state except for the sign difference, indicating the strong magnetic coupling between the Fe and Ge/Te states. The XMCD signal from Fe $L_{2,3}$ edge dominantly probes $3d$ states because of the dipole transition with different azimuthal $\Delta l = l_{\text{final}} - l_{\text{initial}} = +1$. If the spin alignment of different orbitals in two elements is antiparallel, the sign of XMCD signals should be opposite, as long as the sign of Δl for the

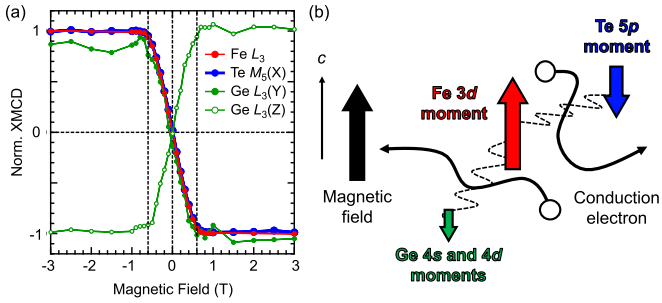

FIG. 4. (a) The magnetic dependence of XMCD signals normalized at the saturated value of each absorption edges. (b) The sketch of the relationship about magnetic moments between Fe 3*d* and seemingly nonmagnetic elements revealed by SX-ARPES and XMCD measurements.

two excitations is the same. The XMCD signal from the Te $M_{4,5}$ edge mainly detects excited 5*p* states with $\Delta l = -1$ and its sign is the same as that of the Fe $L_{2,3}$ edge. This means that the spin polarization of the Te 5*p* state is antiparallel to the Fe 3*d* states. On the other hand, the XMCD signal for the Ge $L_{2,3}$ edge has two signals with different signs (assigned as Y and Z). This can be coherently understood by considering different Δl involved in the two-excitation process, since the sign of the XMCD signals can be flipped with opposite sign of Δl. Compared with the previous XMCD studies for the Ge $L_{2,3}$ edge [46], the XMCD signals at Y and Z are from the final states of $4s(\Delta l = -1)$ and $4d$ $(\Delta l = +1)$, respectively. Therefore, in addition to Te 5*p*, Ge 4*s*/4*d* also has spin-polarized states with its spin alignment antiparallel to those of Fe 3*d* under external magnetic field, which is summarized schematically in Fig. 4(b). While macroscopic moment originates mainly from localized Fe spins, such XMCD signal points out that spin-polarized metallic ligand band should play a major role for mediating itinerant ferromagnetism.

Surprisingly large XMCD signal from Te M_5 edge is an important fact. The strength of XMCD signal is defined as $(\mu^- - \mu^+)/(\mu^- + \mu^+ - \text{B.G.})$, and the extracted value for Fe, Ge, Te signal from ligand Te 5*p* reaches to the value of Fe L_3 edge, where B.G. means the background. So far, the similarly defined finite XMCD signal strength from nonmagnetic element has been reported in various literature [22,47–56]. However, as far as we recognize, our value of ∼30% XMCD signal for nonmagnetic element is much larger than previous reports for different materials unlimited in vdW coupled systems. Our findings collectively point out that the spin polarization of the delocalized ligand states plays a major role in realizing itinerant long-range ferromagnetism in low-dimensional systems. Indeed, validity of this picture is strongly supported by direct observation of band hybridization and the induced remarkable spin polarization for itinerant ligand Ge/Te states [Fig. 4(a)]. Since spin-polarized density of states for ligand states $N(\uparrow_{\text{major}}) - N(\downarrow_{\text{minor}})$ at E_F is expected to be higher when the hybridized flat band is located near E_F, our observation of the flat-band energy at $E - E_F \sim -0.3$ eV [see Fig. 1(f)], which is closer to E_F than that of Fe_3GeTe_2 ($E - E_F \sim -0.4$ eV [13]), can explain the higher T_C of Fe_5GeTe_2 than that of Fe_3GeTe_2.

An interesting consequence of observed large XMCD signal for heavy-element Te is the possible major role of spin-orbit (SO) coupling effect for determining detailed arrangement of Fe-derived spins. This hypothesis is in line with the conclusion drawn, for example, in itinerant ferromagnetic system intermetallic iron-based compounds FePt. In this system, large spin polarization of nonmagnetic heavy-element Pt induced by Fe introduces a prominent SO coupling effect to determine spin structure of Fe including magnetic anisotropy [57–59]. As also in vdW ferromagnetic insulators $Cr_2Ge_2Te_6$ [15–19] and CrI_3 [20–22], we think SO coupling plays a major role to determine detailed arrangement of localized spins of Fe in present vdW ferromagnetic metal Fe_5GeTe_2. The information obtained in this study will be essential for understanding of temperature-dependent unique physical properties, instead of simple ferromagnetism, including formation of ferrimagnetism, Fano-shaped near E_F electronic state, noncollinear spin structure, and their exotic temperature evolution of domain structuring [26,27,60,61]. In particular, we think Fe(1) plays an important role for controlling physical properties in Fe_5GeTe_2 through hybridization with heavy ligand state Te since this magnetic sites is the nearest neighbor for Te site [see Fig. 1(a)] and missing in related material Fe_3GeTe_2 (see Fig. S4 in the Supplemental Material [30,62–67]). The direct visualization of the electronic structure at the Fe-Te hybridized layer would bring a further insight into the vdW ferromagnets in Fe_5GeTe_2, that will be an interesting future study.

In summary, combining ARPES, DFT, and direct observation of elemental selective XMCD measurements, we provide a collective picture of emergent hybridization-driven spin polarization of none-magnetic ligand states. Our discovery of surprisingly large spin polarization of the delocalized ligand Te states points out a major role for realizing itinerant long-range ferromagnetism in low-dimensional systems, while the difficulty of aligning localized Fe 3*d* spins by themselves in a low-dimensional system is expected. Beyond conventional magnetism, controlling magnetism through heavy ligand element is an interesting root for designing emergent itinerant ferromagnetism in low-dimensional systems, including their heterostructures.

We thank M. Kitamura for supporting the XAS/XMCD measurements. The SX-ARPES measurement was performed under the approval of BL25SU at SPring-8 (Proposal No. 2019B1097). The XAS/XMCD measurements were performed under the approval of BL23SU at SPring-8 (Proposals JPMXP09A19AE0036 and JPMXP09A19AE0040). This work was partly supported by Japan Society and Science and Technology Agency (JST) Core Research for Evolution Science and Technology (CREST), Japan, Grant No. JPMJCR18I2. This work was partially supported by JSPS KAKENHI (Grants No. 19H02683, No. 19H01816, and No. 19H05824), Japan. This work was partially supported by the Spintronics Research Network of Japan (Spin-RNJ). Y.Z. acknowledges the Basic Research Funding of IHEP, CAS (Grant No. Y951556). F.C.C. and C.H.H. acknowledge support from the National Center for Theoretical Sciences and the Ministry of Science and Technology of Taiwan

under Grants No. MOST-107-2628-M-110-001-MY3, No. 108-2911-I-110-502, and No. 107-2911-I-110-506. They are also grateful to the National Center for High-performance Computing for computer time and facilities.

[1] E. C. Stoner, Proc. R. Soc. A **165**, 372 (1938).
[2] B. Kim, A. B. Andrews, J. L. Erskine, K. J. Kim, and B. N. Harmon, Phys. Rev. Lett. **68**, 1931 (1992).
[3] A. Kakizaki, K. Ono, K. Tanaka, K. Shimada, and T. Sendohda, Phys. Rev. B **55**, 6678 (1997).
[4] E. Kisker, K. Schroder, M. Campagna, and W. Gudat, Phys. Rev. Lett. **52**, 2285 (1984).
[5] J. Okabayashi, K. Tanaka, M. Hashimoto, A. Fujimori, K. Ono, M. Okusawa, and T. Komatsubara, Phys. Rev. B **69**, 132411 (2004).
[6] D. E. Shai, C. Adamo, D.W. Shen, C. M. Brooks, J.W. Harter, E. J. Monkman, B. Burganov, D. G. Schlom, and K. M. Shen, Phys. Rev. Lett. **110**, 087004 (2013).
[7] Z. Fei, B. Huang, P. Malinowski, W. Wang, T. Song, J. Sanchez, W. Yao, D. Xiao, X. Zhu, A. F. May, W. Wu, D. H. Cobden, J.-H. Chu, and X. Xu, Nat. Mater. **17**, 778 (2018).
[8] K. Kim, J. Seo, E. Lee, K.-T. Ko, B. S. Kim, B. G. Jang, J. M. Ok, J. Lee, Y. J. Jo, W. Kang, J. H. Shim, C. Kim, H. W. Yeom, B. I. Min, B.-J. Yang, and J. S. Kim, Nat. Mater. **17**, 794 (2018).
[9] G. D. Nguyen, J. Lee, T. Berlijn, Q. Zou, S. M. Hus, J. Park, Z. Gai, C. Lee, and A.-P. Li, Phys. Rev. B **97**, 014425 (2018).
[10] Y. Deng, Y. Yu, Y. Song, J. Zhang, N. Z. Wang, Z. Sun, Y. Yi, Y. Z. Wu, S. Wu, J. Zhu, J. Wang, X. H. Chen, and Y. Zhang, Nature (London) **563**, 94 (2018).
[11] C. Gong and X. Zhang, Science **363**, eaav4450 (2019).
[12] Y. Wu, S. Zhang, G. Yin, J. Zhang, W. Wang, Y. L. Zhu, J. Hu, K. Wong, C. Fang, C. Wang, X. Han, Q. Shao, T. Taniguchi, K. Watanabe, J. Zang, Z. Mao, X. Zhang, and K. L. Wang, Nat. Commun. **11**, 3860 (2020).
[13] X. Xu, Y. W. Li, S. R. Duan, S. L. Zhang, Y. J. Chen, L. Kang, A. J. Liang, C. Chen, W. Xia, Y. Xu, P. Malinowski, X. D. Xu, J.-H. Chu, G. Li, Y. F. Guo, Z. K. Liu, L. X. Yang, and Y. L. Chen, Phys. Rev. B **101**, 201104(R) (2020).
[14] N. D. Mermin and H. Wagner, Phys. Rev. Lett. **17**, 1133 (1966).
[15] V. Carteaux, D. Brunet, G. Ouvrard, and G. Andre, J. Phys.: Condens. Matter **7**, 69 (1995).
[16] C. Gong, L. Li, Z. Li, H. Ji, A. Stern, Y. Xia, T. Cao, W. Bao, C. Wang, Y. Wang, Z. Q. Qiu, R. J. Cava, S. G. Louie, J. Xia, and X. Zhang, Nature (London) **546**, 265 (2017).
[17] W. Xing, Y. Chen, P. M. Odenthal, X. Zhang, W. Yuan, T. Su, Q. Song, T. Wang, J. Zhong, S. Jia, X. C. Xie, Y. Li, and W. Han, 2D Mater. **4**, 024009 (2017).
[18] K. Wang, S. Nikolaev, W. Ren, and I. Solovyev, Phys. Chem. Chem. Phys. **21**, 9597 (2019).
[19] M. D. Watson, I. Marković, F. Mazzola, A. Rajan, E. A. Morales, D. M. Burn, T. Hesjedal, G. van der Laan, S. Mukherjee, T. K. Kim, C. Bigi, I. Vobornik, M. C. Hatnean, G. Balakrishnan, and P. D. C. King, Phys. Rev. B **101**, 205125 (2020).
[20] B. Huang, G. Clark, E. Navarro-Moratalla, D. R. Klein, R. Cheng, K. L. Seyler, D. Zhong, E. Schmidgall, M. A. McGuire, D. H. Cobden, W. Yao, D. Xiao, P. Jarillo-Herrero, and X. Xu, Nature (London) **546**, 270 (2017).
[21] J. L. Lado and J. Fernández-Rossier, 2D Mater. **4**, 035002 (2017).
[22] D.-H. Kim, K. Kim, K.-T. Ko, J. H. Seo, J. S. Kim, T.-H. Jang, Y. Kim, J.-Y. Kim, S.-W. Cheong, and J.-H. Park, Phys. Rev. Lett. **122**, 207201 (2019).
[23] V. N. Strocov, L. L. Lev, M. Kobayashi, C. Cancellieri, M.-A. Husanu, A. Chikina, N. B. M. Schröter, X. Wang, J. A. Krieger, and Z. Salman, J. Electron Spectrosc. Relat. Phenom. **236**, 1 (2019).
[24] G. van der Laan and A. I. Figueroa, Coord. Chem. Rev. **277-278**, 95 (2014).
[25] J. Stahl, E. Shlaen, and D. Johrendt Anorg, Allg. Chem. **644**, 1923 (2018).
[26] A. F. May, D. Ovchinnikov, Q. Zheng, R. Hermann, S. Calder, B. Huang, Z. Fei, Y. Liu, X. Xu, and M. A. McGuire, ACS Nano **13**, 4436 (2019).
[27] A. F. May, C. A. Bridges, and M. A. McGuire, Phys. Rev. Materials **3**, 104401 (2019).
[28] K. Momma and F. Izumi, J. Appl. Crystallogr. **44**, 1272 (2011).
[29] Y. Senba, H. Ohashi, Y. Kotani, T. Nakamura, T. Muro, T. Ohkochi, N. Tsuji, H. Kishimoto, T. Miura, M. Tanaka, M. Higashiyama, S. Takahashi, Y. Ishizawa, and T. Matsu, AIP Conf. Proc. **1741**, 030044 (2016).
[30] See Supplemental Material at http://link.aps.org/supplemental/10.1103/PhysRevB.103.L060403 for the detail of experimental methods, the VUV-APRES results, core-level photoemission results, the magneto-optical sum-rules analysis for Fe $L_{2,3}$ edge XAS/XMCD, and computational method.
[31] Y. Saitoh, Y. Fukuda, Y. Takeda, H. Yamagami, S. Takahashi, Y. Asano, T. Hara, K. Shirasawa, M. Takeuchi, T. Tanaka, and H. Kitamura, J. Synchrotron Radiat. **19**, 388 (2012).
[32] J. J. Yeh and I. Lindau, At. Data Nucl. Data Tables **32**, 1 (1985).
[33] One can see a discrepancy between calculated band structure and experimental SX-ARPES. In particular, calculated $|k_{\mathrm{H}}|$ is about twice larger than the experimental result at $|k_{\mathrm{H}}| = 0.38\,\text{Å}^{-1}$. This discrepancy is partly from possible uncertainty in occupancy of Fe(1) sites. While our calculation assumes ideal rhombohedral crystal structure with placing Fe(1) in the unit cell, in real crystal, occupation of Fe(1) is not certain but with keeping total chemical composition approximately Fe_5GeTe_2. We think this discrepancy plays a minor role within the main purpose of this study.
[34] C. T. Chen, Y. U. Idzerda, H.-J. Lin, N. V. Smith, G. Meigs, E. Chaban, G. H. Ho, E. Pellegrin, and F. Sette, Phys. Rev. Lett. **75**, 152 (1995).
[35] S. Ueda, H. Tanaka, J. Takaobushi, E. Ikenaga, J.-J. Kim, M. Kobata, T. Kawai, H. Osawa, N. Kawamura, M. Suzuki, and K. Kobayashi, Appl. Phys. Express **1**, 077003 (2008).
[36] S. Ueda and I. Hamada, J. Phys. Soc. Jpn. **86**, 124706 (2017).
[37] S. Ueda, M. Mizuguchi, M. Tsujikawa, and M. Shiraid, Sci. Technol. Adv. Mater. **20**, 796 (2019).
[38] D. Shirley, Phys. Rev. B **5**, 4709 (1972).

[39] J. Végh, J. Electron Spectrosc. Relat. Phenom. **46**, 411 (1988).
[40] H.-Y. Cheng, C. A. Jong, R.-J. Chung, T.-S. Chin, and R.-T. Huang, Semicond. Sci. Technol. **20**, 1111 (2005).
[41] J. Yu, B. Liu, T. Zhang, Z. Song, S. Feng, and B. Chen, Appl. Surf. Sci. **253**, 6125 (2007).
[42] K. Prabhakaran and T. Ogino, Surf. Sci. **325**, 263 (1995).
[43] Y. Wang, U. Ramesh, C. K. A. Nyamekye, B. J. Ryan, R. D. Nelson, A. M. Alebri, U. H. Hamdeh, A. Hadi, E. A. Smith, and M. G. Panthani, Chem. Commun. **55**, 6102 (2019).
[44] B. T. Thole, P. Carra, F. Sette, and G. van der Laan, Phys. Rev. Lett. **68**, 1943 (1992).
[45] P. Carra, B. T. Thole, M. Altarelli, and X. Wang, Phys. Rev. Lett. **70**, 694 (1993).
[46] J. W. Freeland, R. H. Kodama, M. Vedpathak, S. C. Erwin, D. J. Keavney, R. Winarski, P. Ryan, and R. A. Rosenberg, Phys. Rev. B **70**, 033201 (2004).
[47] D. J. Keavney, D. Wu, J.W. Freeland, E. Johnston-Halperin, D. D. Awschalom, and J. Shi, Phys. Rev. Lett. **91**, 187203 (2003).
[48] T. Okane, J. Okamoto, K. Mamiya, S. Fujimori, Y. Takeda, Y. Saitoh, Y. Muramatsu, A. Fujimori, Y. Haga, E. Yamamoto, A. Tanaka, T. Honma, Y. Inada, and Y. Onuki, J. Phys. Soc. Jpn. **75**, 024704 (2006).
[49] D. Haskel, Y. B. Lee, B. N. Harmon, Z. Islam, J. C. Lang, G. Srajer, Ya. Mudryk, K. A. Gschneidner, and V. K. Pecharsky, Phys. Rev. Lett. **98**, 247205 (2007).
[50] P. Wadley, A. A. Freeman, K. W. Edmonds, G. van der Laan, J. S. Chauhan, R. P. Campion, A. W. Rushforth, B. L. Gallagher, C. T. Foxon, F. Wilhelm, A. G. Smekhova, and A. Rogalev, Phys. Rev. B **81**, 235208 (2010).
[51] B. G. Ueland, A. Pandey, Y. Lee, A. Sapkota, Y. Choi, D. Haskel, R. A. Rosenberg, J. C. Lang, B. N. Harmon, D. C. Johnston, A. Kreyssig, and A. I. Goldman, Phys. Rev. Lett. **114**, 217001 (2015).
[52] M. Ye, W. Li, S. Zhu, Y. Takeda, Y. Saitoh, J. Wang, H. Pan, M. Nurmamat, K. Sumida, F. Ji, Z. Liu, H. Yang, Z. Liu, D. Shen, A. Kimura, S. Qiao, and X. Xie, Nat. Commun. **6**, 8913 (2015).
[53] K. Nagai, H. Fujiwara, H. Aratani, S. Fujioka, H. Yomosa, Y. Nakatani, T. Kiss, A. Sekiyama, F. Kuroda, H. Fujii, T. Oguchi, A. Tanaka, J. Miyawaki, Y. Harada, Y. Takeda, Y. Saitoh, S. Suga, and R. Y. Umetsu, Phys. Rev. B **97**, 035143 (2018).
[54] A. Tcakaev, V. B. Zabolotnyy, R. J. Green, T. R. F. Peixoto, F. Stier, M. Dettbarn, S. Schreyeck, M. Winnerlein, R. Crespo Vidal, S. Schatz, H. B. Vasili, M. Valvidares, K. Brunner, C. Gould, H. Bentmann, F. Reinert, L. W. Molenkamp, and V. Hinkov, Phys. Rev. B **101**, 045127 (2020).
[55] F. Wilhelm, J. P. Sanchez, J.-P. Brison, D. Aoki, A. B. Shick, and A. Rogalev, Phys. Rev. B **95**, 235147 (2017).
[56] V. M. Pereira, S. G. Altendorf, C. E. Liu, S. C. Liao, A. C. Komarek, M. Guo, H.-J. Lin, C. T. Chen, M. Hong, J. Kwo, L. H. Tjeng, and C. N. Wu, Phys. Rev. Materials **4**, 064202 (2020).
[57] I. V. Solovyev, P. H. Dederichs, and I. Mertig, Phys. Rev. B **52**, 13419 (1995).
[58] S. Ueda, M. Mizuguchi, Y. Miura, J. G. Kang, M. Shirai, and K. Takanashi, Appl. Phys. Lett. **109**, 042404 (2016).
[59] K. Ikeda, T. Seki, G. Shibata, T. Kadono, K. Ishigami, Y. Takahashi, M. Horio, S. Sakamoto, Y. Nonaka, M. Sakamaki, K. Amemiya, N. Kawamura, M. Suzuki, K. Takanashi, and A. Fujimori, Appl. Phys. Lett. **111**, 142402 (2017).
[60] T. Ohta, K. Sakai, H. Taniguchi, B. Driesen, Y. Okada, K. Kobayashi, and N. Niimi, Appl. Phys. Express **13**, 043005 (2020).
[61] H. Zhang, R. Chen, K. Zhai, X. Chen, L. Caretta, X. Huang, R. V. Chopdekar, J. Cao, J. Sun, J. Yao, R. Birgeneau, and R. Ramesh, Phys. Rev. B **102**, 064417 (2020).
[62] P. Hohenberg and W. Kohn, Phys. Rev. **136**, B864 (1964).
[63] J. P. Perdew, K. Burke, and M. Ernzerhof, Phys. Rev. Lett. **77**, 3865 (1996).
[64] P. E. Blöchl, Phys. Rev. B **50**, 17953 (1994).
[65] G. Kresse and D. Joubert, Phys. Rev. B **59**, 1758 (1999).
[66] G. Kresse and J. Hafner, Phys. Rev. B **47**, 558 (1993).
[67] G. Kresse and J. Furthmüller, Phys. Rev. B **54**, 11169 (1996).